Thermally activated transitions in a bistable three-dimensional optical trap

Lowell I. McCann†, Mark Dykman & Brage Golding

Department of Physics and Astronomy, Michigan State University, East Lansing, Michigan 48824-1116, USA

Activated escape from a metastable state underlies many physical, chemical and biological processes: examples include diffusion in solids, switching in superconducting junctions[1,2], chemical reactions[3,4] and protein folding[5,6]. Kramers presented the first quantitative calculation[7] of thermally driven transition rates in 1940. Despite widespread acceptance of Kramers' theory[8], there have been few opportunities to test it quantitatively as a comprehensive knowledge of the system dynamics is required. A trapped brownian particle (relevant to our understanding of the kinetics, transport and mechanics of biological matter[9,10]) represents an ideal test system. Here we report a detailed experimental analysis of the brownian dynamics of a sub-micrometre sized dielectric particle confined in a double-well optical trap. We show how these dynamics can be used to directly measure the full three-dimensional confining potential—a technique that can also be applied to other optically trapped objects[11,12]. Excellent agreement is obtained between the predictions of Kramers' theory and the measured transition rates, with no adjustable or free parameters over a substantial range of barrier heights.

A mesoscopic particle, suspended in a liquid and confined within a metastable potential well provides an ideal representation of Kramers' ideas. The particle moves at random within the well until a large fluctuation propels it out of the well over an energy barrier. The potential can be created with a gradient optical trap—a technique widely used in biophysical studies[9]. Dual optical traps were introduced initially to study the synchronization of the interwell transitions by periodic forcing[13]. A particle in a dual optical trap is a well-controlled model system which can be used to address quantitatively the problem of transition rates provided the confining potential can be accurately determined.

The optically induced potential wells constructed in the present experiments are formed by focusing two parallel laser beams through a single objective lens. Each beam creates a stable three-dimensional trap as a result of electric field gradient forces exerted on a transparent dielectric spherical silica particle of diameter $2R = 0.6\,\mu$m (Bangs Laboratories). Displaced by 0.25 to 0.45 μm, the beams create a double-well potential, with the stable positions of the particle centre at $\mathbf{r}_1$ and $\mathbf{r}_2$. Relatively infrequent random transitions between the potential wells occur through a saddle point at $\mathbf{r}_s$ as depicted in Fig. 1a. Both the depth of each potential well and the height of the intervening barrier are under experimental control.

The two HeNe lasers (17 mW, 633 nm) that create the traps are stabilized by Pockels cell electro-optic modulators and imaged into a sample cell by a 100x 1.4 NA PlanApo objective lens mounted in an Olympus IX-70 microscope. The beams are mutually incoherent and circularly polarized as they enter the microscope. A single trapped sphere is imaged onto a Dalsa CA-D1 CCD camera operated at 200 frames per second. The coordinates of the sphere's centre in the focal plane of the objective lens are found to within ±10 nm with a pattern-matching routine, and the coordinate in the beams' propagation direction is extracted by analysis of the image size as it moves above and below the focal plane. The sealed sample cell, constructed from two glass coverslips and epoxy resin, holds a dilute suspension of silica spheres in water at room temperature. The experimental output of this system is a time record of the coordinates $\mathbf{r}(t)$; as shown in Fig. 1b.

As a result of the short equilibration time of the sphere in water ($\gamma^{-1} = M/(6\pi\eta R) \sim 10^{-7}$ s, where η is the viscosity of water and M is the particle mass), the brownian particle relaxes to equilibrium on a timescale much shorter than the sampling time. The spatial probability density is therefore:

$$\rho(\mathbf{r}) = Z^{-1}\exp(-U(\mathbf{r})/k_BT) \quad (1)$$

Here $U(\mathbf{r})$ is the potential energy as a function of particle position, and Z is a normalization constant. The probability density is found from the time series $\mathbf{r}(t)$, typically using 10^6 to 10^7 frames, for durations much longer than the mean interwell transition times. Equation (1) then allows us to obtain the potential directly from measurements.

Figure 2 shows $U(\mathbf{r})$ for a two-beam trap. We choose the x axis to be in the direction from one beam to the other and the z axis along the propagation direction of the beams. The potential minima, $\mathbf{r}_1$ and $\mathbf{r}_2$, lie in the symmetry plane $y = 0$ formed by the beam axes. Figure 2a shows a two-dimensional cross-section, at y=0, of the potential with energy contours at 1.0 k_BT intervals distinguished by colour-coding, where k_B is the Boltzmann constant and T is temperature. If, for a given x, we find the minimum of U($\mathbf{r}$) over y and z, we obtain the familiar one-dimensional representation of a double-well potential shown in Fig. 2b. Figure 2c shows the energy contours at $\mathbf{r}_2$ for a cross-section in the y–z plane with the corresponding energy profile in Fig. 2d. The elongated profile along z is expected, since the radial field gradient is determined by the transverse beam profile whereas the weaker axial gradient depends on the angular divergence of the focused beam near its diffraction-limited waist[14].

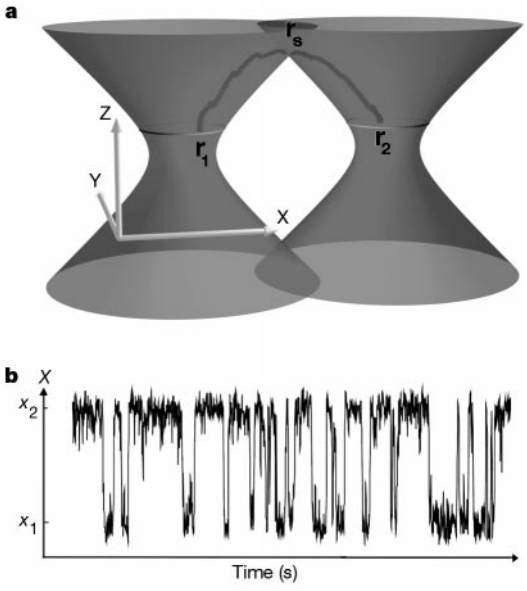

Figure 1 Interwell transitions in a dual optical trap. **a**, Two neighbouring focused beams in the absence of a perturbing trapped sphere are shown. The dark line illustrates the path of a trapped sphere in an interwell transition between $\mathbf{r}_1$ and $\mathbf{r}_2$ through the saddle at $\mathbf{r}_s$. The equilibrium positions $\mathbf{r}_1$ and $\mathbf{r}_2$, at the level of the rings around the beams, are displaced above the focal plane of the incident beams. **b**, Projection of particle trajectory on the x-axis perpendicular to the beams, where x_1, x_2 are components of $\mathbf{r}_1$, $\mathbf{r}_2$. The sampling interval is 5 ms and the total time duration of the record is approximately 8 s. During the acquisition time, a computer performs a pattern-matching routine that returns the three particle coordinates. The particle spends most of its time in the vicinity of the stable points $\mathbf{r}_1$ and $\mathbf{r}_2$ with infrequent transitions between them.

† Present address: Department of Physics, University of Wisconsin-River Falls, River Falls, Wisconsin 54022, USA.

Table 1 Features of the optical potential in Fig. 2 and associated transition rates

	$\lvert\omega^{(1)}\rvert$	$\omega^{(2)}$	$\omega^{(3)}$	$\Delta U/k_BT$	W_0^K	W^K	W^{meas}
Well at $\mathbf{r}_1$	16 ± 4	55 ± 14	6 ± 3	2.77 ± 0.05	80 ± 40	5 ± 2	6.57 ± 0.03
Saddle at $\mathbf{r}_s$	7 ± 2	50 ± 25	6 ± 3				
Well at $\mathbf{r}_2$	21 ± 5	56 ± 14	6 ± 3	3.51 ± 0.04	110 ± 50	3 ± 2	3.70 ± 0.02

Characteristic frequencies $\omega_i^{(j)}$ (in 10^4 s^{-1}, with $j = 1, 2, 3$) associated with the extrema, $\mathbf{r}_i$, of the potential in Fig. 2. Note that $\omega_s^{(1)2} < 0$. W_0^K is the Kramers prefactor, W^K is the Kramers rate, and W^{meas} is the experimentally determined rate in transitions per second, reported for the two potential wells at $\mathbf{r}_1$ and $\mathbf{r}_2$. $\Delta U/k_BT$ is the reduced barrier height. The errors reported for $\omega^{(3)}$ do not include the uncertainty in the z-position calibration since it does not influence the value of W_0^K.

The double-well potential in Fig. 2 has minima $\mathbf{r}_{1,2}$ separated by $\delta x = 0.35$ μm, a single intervening saddle point at $\mathbf{r}_s$, and $U(\mathbf{r}_2) - U(\mathbf{r}_1) = 0.8\ k_BT$. We emphasize that the potential measured in this manner is the overall effective potential experienced by the particle in its environment.

A feature of the effective potential evident in Fig. 2a is the strong symmetry breaking about the focal plane, which is the symmetry plane of the beams, unperturbed by the particle. This symmetry breaking leads to the single saddle point in $U(\mathbf{r})$ instead of two saddle points as might be inferred from Fig. 1a. This aspect of the potential is not an artefact of specific experimental conditions, such as non-parallel optical beams, but is a consequence of the beam–particle interaction. The dielectric particle acts as a spherical lens to refocus the beam inside the sphere. When the particle is displaced in the $+z$ direction above the focal plane, the electromagnetic field is most strongly 'squeezed' into the particle, thus minimizing the total free energy of the polarized particle in the field.

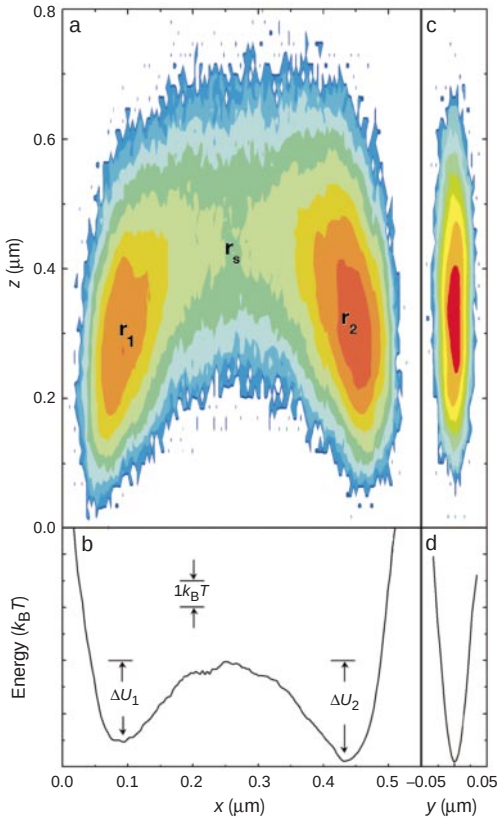

Figure 2 Experimentally determined potential energy of the particle in a double-well optical trap. **a**, Energy contours for a cross-section in the x–z plane that contains the stable points $\mathbf{r}_1$ and $\mathbf{r}_2$, and the saddle point $\mathbf{r}_s$. Each colour indicates a 1.0 k_BT energy interval. **b**, The energy, minimized with respect to y and z, as a function of x as shown in **a**. ΔU_1 and ΔU_2 are the barrier heights for the corresponding wells. **c**, The energy contours in a y–z cross-section containing point $\mathbf{r}_2$. **d**, The energy, minimized with respect to x and z, as a function of y as shown in **c**. The potential described in the figure was extracted from a data set of 4 x 10^6 camera frames containing 94,000 interwell transitions.

In the vicinity of $\mathbf{r}_1$, $\mathbf{r}_2$, and $\mathbf{r}_s$, the potential $U(\mathbf{r})$ is quadratic in the displacements $\delta\mathbf{r} = \mathbf{r} - \mathbf{r}_i$ with i=1,2, or s:

$$U(\mathbf{r}) = U(\mathbf{r}_i) + \frac{1}{2}M\sum_{\alpha,\beta}\Lambda_i^{\alpha\beta}\delta r_\alpha \delta r_\beta \qquad (2)$$

Here $\alpha, \beta = x, y, z$. In practice, we perform a least-squares fit of equation (2) to the data in the vicinity of $\mathbf{r}_i$. As an example of the results and errors in this procedure, Table 1 shows the eigenvalues ω_i^2 of the matrix Λ_i for the potential shown in Fig. 2. The characteristic frequencies $|\omega_i|$ are small compared to the damping rate γ so the particle is overdamped.

We now consider the interwell dynamics of the particle. Specifically, we examine the rates W_{12} (W_{21}) of transitions $1 \rightarrow 2$ ($2 \rightarrow 1$), and their dependence on the energy barriers $\Delta U_1 = U(\mathbf{r}_s) - U(\mathbf{r}_1)$ and $\Delta U_2 = U(\mathbf{r}_s) - U(\mathbf{r}_2)$. We tune $\Delta U_i/k_BT$ up to 8.5 by adjusting the optical intensity in each beam and the beam separation. The presence of the energy asymmetry $\Delta U_{12} = U(\mathbf{r}_2) - U(\mathbf{r}_1)$ between 0.5–3 k_BT allows us to measure two independent rates with a single optical configuration. For each set of experimental conditions, we determine the full three-dimensional potential, similar to Fig. 2. To obtain satisfactory statistics, we accumulated between 2,400 and 94,000 interwell transitions that occurred over 5×10^5 to 10^7 frames.

A quantitative description of thermally activated escape from a one-dimensional metastable potential was given by Kramers[7] and subsequently extended to multidimensional potentials[15]. The subject has been extensively reviewed[8,16,17]. For an overdamped brownian particle in a potential $U(\mathbf{r})$, the Kramers transition rate is:

$$W^K = W_0^K \exp\left(-\frac{\Delta U}{k_BT}\right) \qquad (3)$$

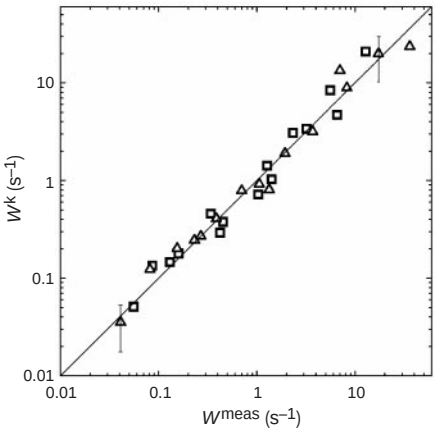

Figure 3 Experimental and theoretical transition rates. We compare the directly measured transition rates, W^{meas}, with the rates calculated from the three-dimensional Kramers theory, W_K, using the measured curvatures of the potential wells. The squares represent escapes from the well at $\mathbf{r}_1$ and the triangles represent escapes from the well at $\mathbf{r}_2$. The line of slope unity indicates the result expected if the data coincide with the Kramers theory.

Here the prefactor is given by the following expression for a three-dimensional potential[15]:

$$W_0^{\mathrm{K}} = \frac{|\omega_{\mathrm{s}}^{(1)}|\omega^{(1)}}{2\pi\gamma}\frac{\omega^{(2)}\omega^{(3)}}{\omega_{\mathrm{s}}^{(2)}\omega_{\mathrm{s}}^{(3)}} \quad (4)$$

Here $\omega_{\mathrm{s}}^{(j)}$and $\omega^{(j)}$characterize, respectively, the curvatures of the potential at the saddle point and at the minimum from which the system escapes, with $(\omega_{\mathrm{s}}^{(1)})^2 < 0$. Therefore, with knowledge of the potential, not only the exponential term, but also the prefactor can be explicitly computed, as shown in Table 1.

Figure 3 shows a plot of the Kramers rates, W^{K}, calculated from equations (3) and (4) as a function of the transition rates, W^{meas}, obtained from the mean dwell time in each state or by fitting an exponential to a histogram of dwell times, in accordance with a Poisson distribution, which yielded equivalent results. The systematic variation of the potential barrier ΔU by approximately 6 $k_{\mathrm{B}}T$ is responsible for the nearly three-decade variation in transition rates. The solid line with unity slope denotes the coincidence of theory and experiment. The data fall remarkably close to the line, confirming the multidimensional Kramers theory of transition rates.

One of the major contributors to the uncertainty in calculating $W^{\mathrm{K}}$is the error in the saddle point frequencies entering equation (4). This is primarily statistical, since the particle spends little time in the vicinity of $\mathbf{r}_{\mathrm{s}}$. This error is amplified for the highest barriers with the lowest transition rates. At low barriers, the statistical uncertainty is small since the transition rates are large, but the Kramers theory is not strictly valid here. If the thermal diffusion length exceeds the size of the parabolic region in the vicinities of the stationary states, then the transition rates are affected by the shape of the potential away from the stationary states. However, the corrections to the theory are small in the range of parameters studied here.

Detailed knowledge of the overall potential, as afforded by our experiments, should enable investigations of the escape rate of underdamped particles in the region in which escape occurs by diffusion over energy, as well as the Kramers turnover region[8,18]. This can be accomplished with present methods by reducing the viscous damping on the particle. Knowledge of the potential is also crucial for understanding strategies for control of escape. Escape occurs by large fluctuations[19] that move the system from a minimum of the potential to the barrier top along optimal paths. The results of this work make it possible to find these paths, enabling selective control of escape rates by external modulating fields[20].

Received 12 August ; accepted 7 October 1999.

1. Han, S., Lapoint, J. & Lukens, J. E. Effect of a two-dimensional potential on the rate of thermally induced escape over the potential barrier. *Phys. Rev. B* **46,** 6338–6345 (1992).
2. Devoret, M. H., Esteve, D., Martinis, J. M., Cleland, A. & Clarke, J. Resonant activation of a brownian particle out of a well: microwave-enhanced escape from the zero-voltage state of a Josephson junction. *Phys. Rev. B* **36,** 58–73 (1987).
3. van Kampen, N. G. *Stochastic Processes in Physics and Chemistry* (Elsevier, Amsterdam, 1992).
4. Gillespie, D. T. Exact stochastic simulation of coupled chemical reactions. *J. Chem. Phys.* **81,** 2340–2361 (1977).
5. Sali, A., Shakhnovich, E. & Karplus, M. How does a protein fold? *Nature* **369,** 248–251 (1994).
6. White, S. H. & Wimley, W. C. Membrane protein folding and stability: Physical principles. *Annu. Rev. Biophys. Biomol. Struct.* **28,** 319–365 (1999).
7. Kramers, H. A. Brownian motion in a field of force and the diffusion model of chemical reactions. *Physica* **7,** 284–304 (1940).
8. Melnikov, V. I. The Kramers problem: fifty years of development. *Phys. Rep.* **209,** 2–71 (1991).
9. Mehta, A. D., Reif, M., Spudich, J. A., Smith, D. A. & Simmons, R. M. Single molecule biomechanics with optical methods. *Science* **283,** 1689–1695 (1999).
10. Smith, D. E., Babcock, H. P. & Chu, S. Single-polymer dynamics in steady shear flow. *Science* **283,** 1724–1727 (1999).
11. Svoboda, K., Schmidt, C. F., Schnapp, B. J. & Block, S. M. Direct observation of kinesin stepping by optical trapping interferometry. *Nature* **365,** 721–727 (1993).
12. Tskhovrebova, L., Trinick, J., Sleep, J. A. & Simmons, R. M. Elasticity and unfolding of single molecules of the giant muscle protein titin. *Nature* **387,** 308–312 (1997).
13. Simon, A. & Libchaber, A. Escape and synchronization of a brownian particle. *Phys. Rev. Lett.* **68,** 3375–3378 (1992).
14. Ghislain, L. P., Switz, N. A. & Webb, W. W. Measurement of small forces using an optical trap. *Rev. Sci. Instrum.* **65,** 2762–2768 (1994).
15. Landauer, R. & Swanson, J. A. Frequency factors in the thermally activated process. *Phys. Rev.* **121,** 1668–1674 (1961).
16. Risken, H. *The Fokker-Planck Equation* (Springer, Berlin, 1989).
17. Hänggi, P., Talkner, P. & Borkovec, M. Reaction-rate theory: fifty years after Kramers. *Rev. Mod. Phys.* **62,** 251–341 (1990).
18. Linkwitz, S., Grabert, H., Turlot, E., Esteve, D. & Devoret, M. H. Escape rates in the region between the Kramers limits. *Phys. Rev. A* **45,** R3369–R3372 (1992).
19. Luchinsky, D. G. & McClintock, P. V. E. Irreversibility of classical fluctuations studied in analogue electrical circuits. *Nature* **389,** 463–466 (1997).
20. Smelyanskiy, V., Dykman, M. I. & Golding, B. Time oscillations of escape rates in periodically driven systems. *Phys. Rev. Lett.* **82,** 3193–3197 (1999).

Acknowledgements

We thank R. Kruse for his assistance with the experiment and graphics. Support from the Center for Fundamental Materials Research at Michigan State University and from the NSF Division of Physics, and Division of Materials Research is gratefully acknowledged.

Correspondence and requests for materials should be addressed to B.G. (email: golding@pa.msu.edu).

Injection and detection of a spin-polarized current in a light-emitting diode

R. Fiederling, M. Keim, G. Reuscher, W. Ossau, G. Schmidt, A. Waag & L. W. Molenkamp

Physikalisches Institut, EP III, Universität Würzburg, 97074 Würzburg, Germany

The field of magnetoelectronics has been growing in practical importance in recent years[1]. For example, devices that harness electronic spin—such as giant-magnetoresistive sensors and magnetoresistive memory cells—are now appearing on the market[2]. In contrast, magnetoelectronic devices based on spin-polarized transport in semiconductors are at a much earlier stage of development, largely because of the lack of an efficient means of injecting spin-polarized charge. Much work has focused on the use of ferromagnetic metallic contacts[3,4], but it has proved exceedingly difficult to demonstrate polarized spin injection. More recently, two groups[5,6] have reported successful spin injection from an NiFe contact, but the observed effects of the spin-polarized transport were quite small (resistance changes of less than 1%). Here we describe a different approach, in which the magnetic semiconductor $Be_xMn_yZn_{1-x-y}Se$ is used as a spin aligner. We achieve injection efficiencies of 90% spin-polarized current into a non-magnetic semiconductor device. The device used in this case is a GaAs/AlGaAs light-emitting diode, and spin polarization is confirmed by the circular polarization state of the emitted light.

The quaternary II–VI magnetic semiconductor $Be_xMn_yZn_{1-x-y}Se$ has particular properties that make it ideally suitable as a spin-aligner for injecting electrons into GaAs. If its lattice parameter is kept constant and matched to the lattice constant of the GaAs substrate, then the Mn concentration can be varied over a wide range. The magnetic Mn ions are incorporated isoelectronically, and the conductivity type can be controlled by external dopants. This is in contrast to, for example, the III–V counterpart $Ga_xMn_{1-x}As$, where the incorporation of Mn inherently leads to a high p-type doping[7] . Here we used n-type $Be_xMn_yZn_{1-x-y}Se$ as the spin-aligning material. Spin-injection of electrons rather than holes is advantageous because of the reduced spin–orbit coupling in the conduction band, decreasing spin decoherence. From the electrical point of view, $Be_xMn_yZn_{1-x-y}Se$ is also ideally suited as a spin-aligner on a GaAs-based heterostructure, as it allows for high quality